ACS APPLIED MATERIALS & INTERFACES

Research Article

Cite This: ACS Appl. Mater. Interfaces 2019, 11, 24360−24366

www.acsami.org

Reversible Modification of Nitrogen-Doped Graphene Based on Se−N Dynamic Covalent Bonds for Field-Effect Transistors

Nannan Zheng,[†] Yiyu Feng,*[,†] Yu Zhang,[‡] Rongjin Li,[‡] Ce Bian,[§] Lihong Bao,[§] Shixuan Du,[§] Huanli Dong,[∥] Yongtao Shen,[†] and Wei Feng*[,†,⊥]

[†]School of Materials Science and Engineering, Tianjin Key Laboratory of Composite and Functional Materials, Key Laboratory of Advanced Ceramics and Machining Technology, Ministry of Education and [‡]Department of Chemistry, School of Sciences, Tianjin University, Tianjin 300072, P. R. China

[§]Institute of Physics & University of Chinese Academy of Sciences and [∥]Institute of Chemistry, Chinese Academy of Sciences, Beijing 100190, P. R. China

[⊥]Collaborative Innovation Center of Chemical Science and Engineering (Tianjin), Tianjin 300072, P. R. China

S *Supporting Information*

ABSTRACT: Temperature-dependent modification is an effective way to reversibly tailor graphene's electronic properties. We present the reversible modification of a uniform monolayer nitrogen-doped graphene (NG) film by the formation and cleavage of temperature-dependent Se−N dynamic covalent bonds. The increasing binding energy in X-ray photoelectron spectroscopy (XPS) indicates that phenylselenyl bromine (PhSeBr) bonds with pyridinic N and pyrrolic N rather than graphitic N by accepting the lone pair of electrons. The temperature dependence of Raman spectra (the increasing D band and the shifts of the 2D band) and XPS spectra (Se 3d and N 1s) indicates that the Se−N dynamic covalent bond is gradually cleaved by treatment at increasing temperatures and is also recovered by the reversible modification. Field-effect transistors (FETs) based on Se−NG exhibit a temperature-dependent change from n-type to p-type conduction and tunable electron and hole mobilities owing to the reversible formation or cleavage of Se−N dynamic covalent bonds. This result opens up opportunities for reversibly controlling electrical properties of FETs by optimizing dynamic covalent bonds.

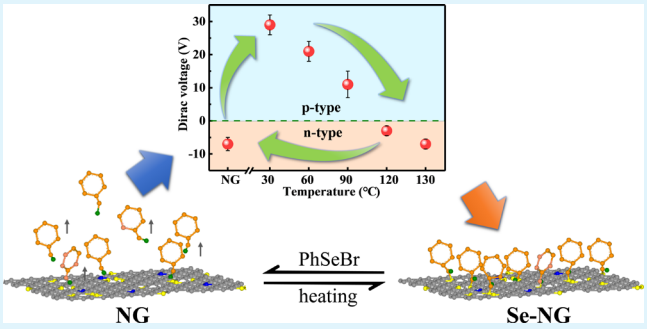

KEYWORDS: *nitrogen-doped graphene, monolayer, dynamic covalent bonds, temperature-dependent, field-effect transistors*

1. INTRODUCTION

Surface modification is one of the most effective ways for chemically tailoring graphene's electronic properties[1−5] such as band gap, Fermi level, and carrier mobility. Recently, the reversible modification of a specific or selected area of graphene has attracted more attention owing to its potential possibility to change electronic properties under external stimuli such as temperature, force, and humidity. Although significant progress has been achieved, such as chemical grafting,[6−11] atomic substitution,[12−20] and adsorption,[21−26] the controllability and reversibility of these modifications remain the key issues to be addressed toward the surface modifications of graphene. To date, controlling the site for chemical reaction, doping, or molecule adsorption on graphene has been a great challenge. Such a problem basically limits the application of modified or doped graphene in environment-responsive devices.

One important way to reversibly modify graphene is to react chemically with specific atoms or chemical groups. Chemical bonding determines the controllability[27,28] and reversibility of the modification. Among potential bonds, dynamic covalent bonds show distinct advantages. The general concept[29] of dynamic covalent bonds shows that the formation of the above bonds can be achieved reversibly under the conditions of equilibrium control. The most common ones are −C═N−, −S−S−, and −Se−N−. Dynamic covalent bonds combine the supramolecular effect and the stability of covalency. Besides, they usually exhibit high selectivity based on unique reactions. Furthermore, dynamic covalent bonds can reversibly respond to external stimuli by forming under one condition and cleaving under another condition. The formation and cleavage are easily controlled under equilibrium-controlled conditions such as irradiation, heating, humidity, pH, and chemical stimulation.[30,31] As a result, it has potential in reversible surface modification, shape-memory, and self-healing with dynamic covalent bonds. It is possible to tailor graphene's electronic

Received: February 16, 2019
Accepted: June 14, 2019
Published: June 14, 2019

DOI: 10.1021/acsami.9b02989
ACS Appl. Mater. Interfaces 2019, 11, 24360−24366

properties for environment-responsive field-effect transistors (FETs)[32−35] by reversible structural modification using dynamic covalent bonds. Despite great potential, however, owing to the few available active atoms or groups, graphene has seldom been modified via dynamic covalent bonds, nor has its electronic properties been altered by reversible formation and cleavage.

In this paper, we present uniform monolayer NG films modified by PhSeBr to form Se−N dynamic covalent bonds. We treated the Se-modified NG at different temperatures to study the temperature-dependent bonds. The formation and cleavage of Se−N bonds are demonstrated by X-ray photoelectron spectroscopy (XPS) and Raman spectroscopy. FETs using NG and Se-modified NG were also fabricated to investigate its performance. Our results show that Se-modified NG changes from n-type to p-type conduction with tunable electron and hole mobilities by rising-temperature treatment.

2. RESULTS AND DISCUSSION

Nitrogen doping is a significant way to regulate the electronic properties of graphene because of its potential for forming dynamic covalent bonds. The schematic illustration of the reversible modification of NG via temperature-dependent Se−N dynamic covalent bonds is shown in Figure 1. As we know,

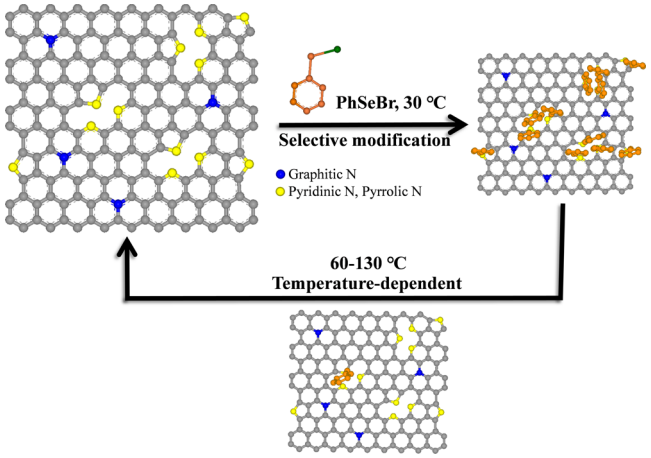

Figure 1. Schematic illustration of the reversible modification of NG via temperature-dependent Se−N dynamic covalent bonds.

NG has three predominant bonding characters for embedded N atoms, including graphitic N, pyridinic N, and pyrrolic N.[36] Rather than graphitic N, the Se atom of a specific selenide can selectively accept the lone-pair electrons of pyridinic N and pyrrolic N and thus form Se−N dynamic covalent bonds. Such Se−N bonds are also easily cleaved at temperatures of >60 °C.[31] As a result, temperature-dependent modification is significant in modulating the electronic properties of graphene at different temperatures.

A large-area (~5.0 cm), single-layer uniform NG film was synthesized by chemical vapor deposition (CVD). Figure S1 schematically illustrates the growth of NG in the double-zone furnace. The uniformity of monolayer NG with low defects was comprehensively controlled by the interrelated growth parameters (see the Experimental Section). Decomposed melamine at high temperature was used as the N-containing carbon source for doping the monolayer NG, and we tried to control the proportion of bonding characters for embedded N atoms in NG by changing the content and decomposition time of melamine. Different bonding characters for embedded N atoms help us to investigate the selectivity, controllability, and temperature dependence of Se−N bonds.

Figure S2 presents the continuous NG film (of centimeter scale) on the copper foil (Figure S2a) and the SiO_2/Si (Figure S2b,c) substrate. The step height on NG was ~1.1 nm (Figure 2a) by the two-dimensional atomic force microscopy (AFM)

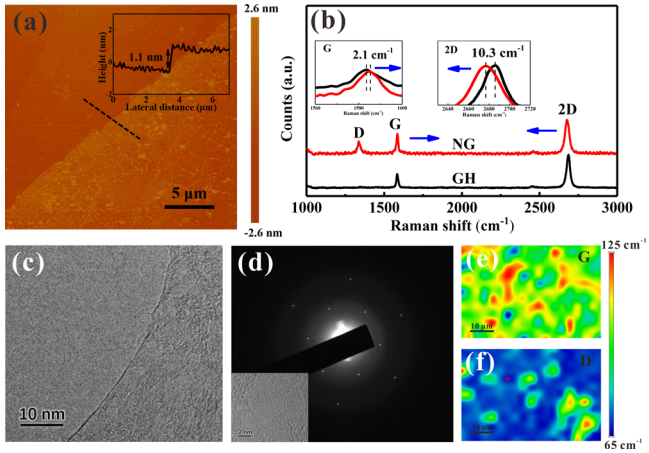

Figure 2. AFM and TEM images and Raman spectra of NG. (a) AFM image of as-synthesized NG films, with a thickness of ~1.1 nm. (b) Raman spectra (at 532 nm excitation) of monolayer NG. (c) High-resolution TEM image of NG. (d) SAED pattern of NG. (e,f) Raman mapping of the NG film (40 × 60 μm^2).

image, which is consistent with monolayer NG in previous studies.[13] The wrinkled or rippled surface might form because of the transfer process. High-resolution transmission electron microscopy (TEM) image is also used to confirm the above analysis. Figure 2c shows that at the edge of the NG film, the existence of the single line reveals the monolayer.[37] A group of selected-area electron diffraction (SAED) patterns were selected from the inset of Figure 2d. The typical hexagonal crystalline structure (Figure 2d) indicates a single-crystalline structure.

Raman spectra of NG and graphene (GH) are illustrated in Figure 2b. In contrast, GH was prepared with methane in the same furnace with NG (see the Experimental Section). The half-peak width of the 2D band and the intensity ratio of the 2D band to the G band (I_{2D}/I_G) are relative to the layers of GH.[38] The monolayer GH usually shows an individual and sharp second-order Raman band with I_{2D}/I_G usually >2.[39] For single-layer doped graphene films, I_{2D}/I_G is usually smaller than that of graphene owing to the present of heteroatoms. After nitrogen doping, I_{2D}/I_G decreases from 2.45 (that of GH) to 1.73 (that of NG) with a slight increase in the half-peak from 26.52 cm^{-1} (GH) to 31.89 cm^{-1} (NG). The sharp 2D band indicates that NG remains as a monolayer structure. Furthermore, NG also exhibits a blue-shifted (2.1 cm^{-1}) G band and a red-shifted (10.3 cm^{-1}) 2D band compared to those of GH, indicating the change of carrier concentration caused by N doping. Electron and hole mobilities tuned by temperature-dependent Se−N bonds are investigated in detail later. Raman mapping images with an area of 40 × 60 μm^2 are also studied (Figure 2e,f). The D band integrated intensity of the NG film indicates well-distributed N doping throughout the nanosheets, and G-band integration suggests a large-scale structure and thickness uniformity of NG. The large-scale

DOI: 10.1021/acsami.9b02989
ACS Appl. Mater. Interfaces 2019, 11, 24360−24366

uniform NG film is an important 2D material for the modification via Se−N dynamic covalent bonds.

We prepared two large-scale uniform NG (NG_1 and NG_2) films with different proportions of bonding characters for embedded N atoms. The element composition and covalent bonding mode of NG were studied by using XPS (Figure S3 for NG_1 and Figure S4 for NG_2). The atomic doping levels were estimated to be 2.8 at. % (NG_1) and 4.0 at. % (NG_2), respectively. Moreover, the fitted peak indicated that NG_1 has four configurations—pyridinic N (14.64 at. %, the value of certain types of N/total N in the NG films), pyrrolic N (54.75 at. %), pyridinic (+H) (9.45 at. %), and graphitic N (21.17 at. %)—whereas two configurations of graphitic N (37.30 at. %) and pyrrolic N (62.69 at. %) are found in NG_2.[40] We investigated the selective bonding between PhSeBr and N atoms and the temperature dependence of Se−N dynamic covalent bonds by tracking changes in the bonding characters. Figure 3a,c shows the N 1s XPS spectra of NG_1, NG_2, Se−

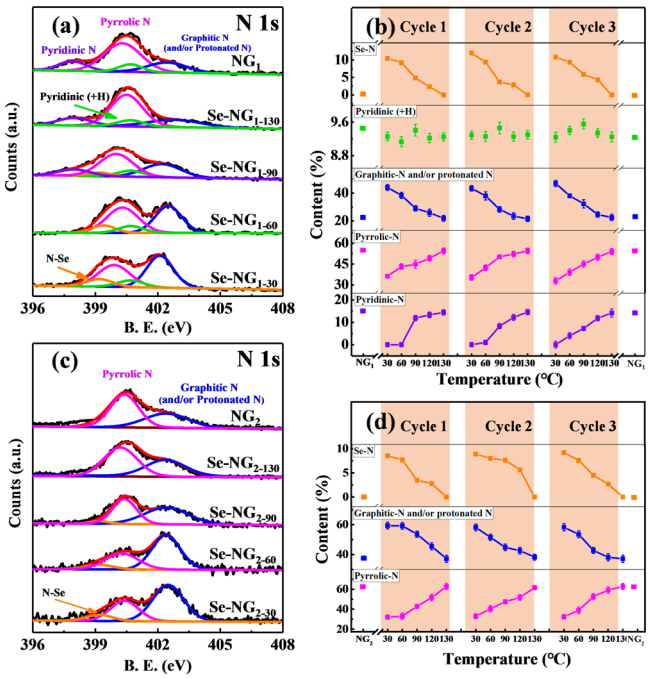

Figure 3. XPS spectra of NG and Se−NG after treatment at different temperatures. (a,c) XPS spectra of N 1s of NG_1, Se−NG_{1-30}, Se−NG_{1-60}, Se−NG_{1-90}, and Se−NG_{1-130}. The fitted curve shows the content of bonding configurations. The pink curve represents pyrrolic N, blue curve represents graphitic N and/or protonated N, purple curve represents pyridinic N, green curve represents pyridinic (+H), and orange curve represents Se−N. (b,d) Changes of different bonding configurations upon three cycles based on the formation and cleavage of Se−N bonds.

NG_1, and Se−NG_2 in the XPS survey spectra, and the corresponding cyclic change of bonding characters after the different-temperature treatments are summarized in Figure 3b,d, respectively. The selenide tends to bond with pyrrolic N and pyridinic N to form Se−N bonds by accepting the nitrogen lone pair electrons. The shared pair of electrons between N and Se atoms leads to an increase of protonated N, which has approximate binding energy to that of graphitic N.[40] Besides, the atomic percentage of Se is 0.42 at. % in Se−NG_1 and 0.48 at. % in Se−NG_2, respectively. The calculation shows that the atomic content ratio of Se to N is 0.15 (Se−NG_1) and 0.12 (Se−NG_2), respectively. According to the fitted XPS curves, Se−N bonds are observed in Se−NG_1 (10.44 at. %) and Se−NG_2 (8.54 at. %). NG_1 and NG_2 shows 1.9 and 2.5 at. % of the sum of pyrrolic N and pyridinic N. In other words, only 0.31−0.36 at. % N atoms are selectively modified by forming Se−N bonds because of the difficulty in distinguishing the difference between pyrrolic N and pyridinic N. Further calculations reveal that Se−NG_1 and Se−NG_2 exhibit an obvious increase in protonated N at 402.4 eV by 22.87 and 22.08 at. % (after subtracting the area percentage of graphitic N and/or protonated N in NG and Se−NG at 30 °C) in the first cycle, respectively. Correspondingly, the intensity of the peak for pyridinic N and pyrrolic N decreases. A relatively larger variation degree in pyridinic N (100%) indicates that it is more favorable for the formation of Se−N bonds compared with pyrrolic N (33.75%). The variation degree is evaluated based on the following equation

$$V = [A_s - A_n]/A_n \times 100\% \quad (1)$$

where A_s and A_n are the area percentage of each type of N before and after modification, respectively. Se−NG_2 also shows a remarkable decrease in the intensity for pyrrolic N by 30.61 at. %. The feature arises from the sp^2-hybridized nitrogen atoms in pyridines offering more electrons than those of pyrrole.[41] Furthermore, the shifts of the Se 3d (Figure S5a) and Br 3d (Figure S5b) indicate the formation of Se−N bonds. However, the Se peak at 55.48 eV shifts to 55.28 eV with a similar shape because of a relatively low amount of Se−N dynamic covalent bonds (0.31−0.36 at. %, average values of three cycles) on NG. Similar shifts of XPS peak are also observed[31] because Se tends to accept electrons with a stronger electronegativity (electron-withdrawing) in the Se−N bonds. Besides, we also demonstrated Se−N-bonding formation by modifying graphene (GH) with PhSeBr under the same condition (the GH film was ultrasound irradiated in a dichloromethane solution containing PhSeBr (0.1 mg/mL) for 1 min and then cleaned with dichloromethane). However, Se 3d and Br 3d are too weak to be detected in the XPS spectra because most PhSeBr only adsorbed on GH can be eliminated during rinsing with dichloromethane. Furthermore, we prepared 2D PhSeBr-adsorbed GH by dropping the PhSeBr solution (0.1 mg/mL) on GH to analyze the potential shift of Se 3d and Br 3d. The peaks of Se 3d (Figure S6a) and Br 3d (Figure S6b) have no obvious change compared with PhSeBr, indicating weak electronic interaction. These results demonstrate that the small shifts of weak Se 3d peaks are mainly due to the formation of Se−N bonds. Figure S5b shows that the binding energy of Br 3d orbitals shifts from 69.88 to 69.08 eV. Thus, after the formation of Se−N covalent bond, Br become the opposite ions of protonated pyridine. According to the literature,[42] there is a remote distance between the Br and Se atom when the Se−N covalent bond formed. Besides, a hydrogen bond might form between Br and adjacent H atoms on the pyridine and benzene ring. Elemental mapping investigates the chemical composition of Se−NG_1 (250 nm × 250 nm, Figure S7a). The elemental mapping images of Se and Br are shown in Figure S7b,c, respectively. It is obvious that Se and Br have a homogeneous distribution with similar intensity, indicating that the Se−N bond does not destroy the basal plane of NG.

We further studied the temperature dependence of Se−N dynamic covalent bonds. The formation and cleavage of the bonds are of great importance for tailoring electronic

DOI: 10.1021/acsami.9b02989
ACS Appl. Mater. Interfaces 2019, 11, 24360−24366

properties reversibly and controllably. The above two kinds of Se−NG films on the SiO_2/Si substrate were treated at 30, 60, 90, 120, and 130 °C for 15 min, respectively (with resulting films referred to as Se−NG_{1-30}, Se−NG_{1-60}, Se−NG_{1-90}, Se−NG_{1-120}, and Se−NG_{1-130} and Se−NG_{2-30}, Se−NG_{2-60}, Se−NG_{2-90}, Se−NG_{2-120}, and Se−NG_{2-130}; see the Experimental Section). After cooling in Ar, we characterized the change of bonding characters for embedded N atoms within the carbon lattice by using their XPS spectra (Tables S1−S3). The change in binding energy illustrates the temperature dependence of the Se−N bonds. With an increase in temperature, the Se−N bonds on NG exhibit an increasing amount of pyrrolic N and pyridinic N owing to the thermally induced cleavage. Meanwhile, we investigated the XPS spectra of (1:1 correspondence) Se 3d, N 1s. As shown in Figure S8, the Se 3d peak (55.48 eV, PhSeBr) shifts to 55.28−55.31 eV (Se−NG_{1-30}, Se−NG_{1-60} and Se−NG_{1-90}) with a similar shape because of the formation of Se−N dynamic covalent bonds. Furthermore, the intensity of the Se 3d peak gradually decreases when Se−NG is treated at a higher temperature because of the cleavage of Se−N covalent bonds. Finally, Se−NG_{1-130} shows no Se peak, which is consistent with that of NG before the modification. The electronic properties of NG can be modulated by temperature-dependent Se−N bonds based on different bonding characters of N atoms. After treatment at 130 °C, Se−NG recovers its original bonding characters before the modification. Moreover, Se−NG_1 and Se−NG_2 both exhibit excellent cycling performance with a slight change in the area percentage of the three different N types for no more than 7.9% after 10 cycles (after subtracting the area percentage of different types of N in NG and Se−NG for each cycles; Figure S9), indicating good controllability and reversibility of the Se−N bonds. This result reveals that the formation and cleavage of temperature-dependent Se−N bonds are independent of bonding characters for embedded N atoms within the carbon lattice.

We further used temperature-dependent Raman spectroscopy to investigate the change in structure and electronic interaction of Se−NG_1 caused by the formation and cleavage of Se−N bonds. The Se−NG_1 film was transferred on the SiO_2/Si base and heated to specific temperatures at the rate of 5 °C/min on a stage. The Raman spectra of Se−NG_{1-30}, Se−NG_{1-60}, Se−NG_{1-90}, and Se−NG_{1-130} are shown in Figure 4a. The intensity ratio of the D band to G band (I_D/I_G) is inverse ratio to La,[43] the average interdefect distance. Consequently,

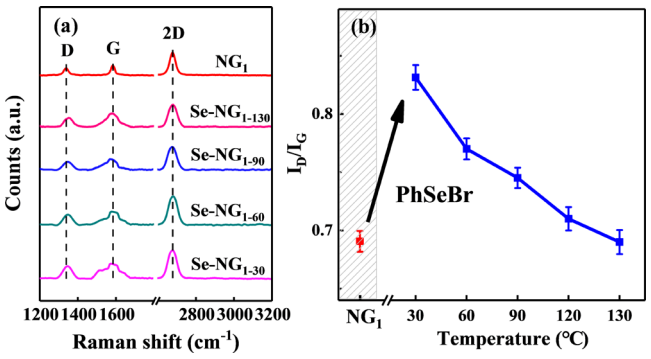

Figure 4. Raman spectra of NG and Se−NG after treatment at different temperatures. (a) Raman spectra of NG_1, Se−NG_{1-30}, Se−NG_{1-60}, Se−NG_{1-90}, and Se−NG_{1-130}. (b) Corresponding ratio of I_D and I_G.

the defects introduced by Se−N bonds can be tracked by the change in I_D/I_G. However, Se−NG_1 exhibits a slight increase in I_D/I_G from 0.69 (NG) to 0.83 (Figure 4b). We infer that because of a low conjugated structure, PhSeBr on the surface is considered as a weak defect for graphene by forming Se−N bonds.[7,44,45] A similar change is also observed by Sarkar,[7] who reported a similar slight increase of I_D/I_G (0.01−0.12) because of surface modification by $Cr(CO)_6$ based on coordination bonds of Cr metal ions. The low-degree modification (0.31−0.36 at. %) of PhSeBr on pyrrolic N and pyridinic N cannot cause a large change in I_D/I_G. Besides, the 2D band at 2677.6 cm^{-1} (NG) shifts to 2679.5 cm^{-1} (Se−NG_{1-30}) by 1.9 cm^{-1} (Figure S10). Such a 2D band gradually returns to 2677.6 cm^{-1} by treatment at increasing temperatures because of the cleavage of Se−N bonds. Despite the reversible change, the shift is insignificant compared with others' work.[28] Such temperature-dependent Se−N bonds change the concentration of electrons. This result is consistent with the temperature-dependent bonding characters for embedded N atoms according to the fitted XPS curves. The structural change was also investigated by Raman mapping images of the D peak intensities of NG_1, Se−NG_{1-30}, Se−NG_{1-60}, Se−NG_{1-90}, and Se−NG_{1-130} at room temperature with an area of 25 × 25 μm^2 (Figure S11). All the images in Figure S11 show the same position. The bright green color (D band) indicates that the D-band intensity of Se−NG decreases gradually with an increase in temperature. The formation and cleavage of temperature-dependent Se−N bonds with great controllability and reversibility enable Se−NG to be fabricated for controlling electrical properties at different temperatures.

To further evaluate the electronic properties, we fabricated a back-gate FET (Figure S12a) on a 1 μm SiO_2/Si/SiO_2 substrate. The Ti/Au film was deposited as the source and drain electrodes. Doped silicon acted as the back gate. An optical micrograph of the device is given in Figure S12b, showing the width and length of the channel. The transfer characteristics curves (I_{ds}−V_g) of the NG and the Se−NG-based FETs are shown in Figure 5a with the source−drain voltage fixed at 500 mV. The NG-based FET exhibits a typical n-type behavior in vacuum at room temperature with a Dirac point at −7 V because part of pyridinic N is hydrogenated [pyridinic (+H)].[46] The output characteristics (I_{ds}−V_{ds}) suggest Ohmic contact between Ti/Au contacts and NG films (Figure S12c). The modification of Se−N dynamic covalent bonds leads to a strong shift of the Dirac point from −7 to 29 V. Besides, Se−NG_{1-30} shows p-type hole conduction behavior by donating lone pairs of electrons of N atoms to form Se−N bonds. Theoretical studies[42] indicate that charge transfers from the lone pair in N to the σ^* orbital of the Se−N bond in the forming processes of Se···N interaction. At the same time, there might be a very low amount of PhSeBr molecules adsorbed on NG during the modification. The Br-ions may also affect the electronic properties of NG by accepting the electron. Because of a relatively strong electronegativity (electron-withdrawing), both Se and Br tend to accept the electron, contributing to p-type doping of NG. As a result, NG show a decreased electron delocalization, leading to p-type doping. The reduced electron concentration and slight increase in defect (PhSeBr) results in an obvious decrease in carrier mobility.

After modification, Se−NG_1 films transferred onto the substrate were heated at 30, 60, 90, 120, and 130 °C in vacuum for 15 min. The performance of FETs was investigated at room

DOI: 10.1021/acsami.9b02989
ACS Appl. Mater. Interfaces 2019, 11, 24360−24366

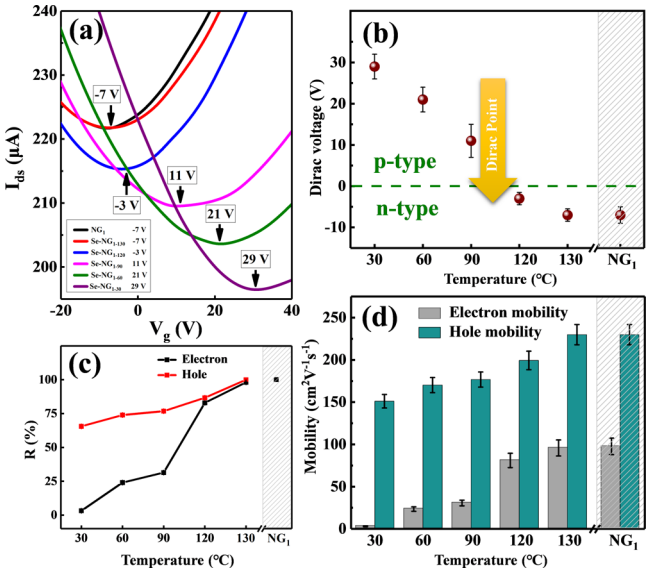

Figure 5. Electrical properties of FETs using NG and Se−NG. (a) Transfer characteristic of NG_1, Se−NG_{1-30}, Se−NG_{1-60}, Se−NG_{1-90}, Se−NG_{1-120}, and Se−NG_{1-130} FETs. (b) Changed voltage of the Dirac point. (c,d) Corresponding ratio of electron and hole mobilities after treatment at different temperatures.

temperature. According to Figure 5b, the formation and cleavage of Se−N bonds can reversibly tailor the electronic properties of NG such as transport behavior and carrier mobility. The Dirac point gradually shifts to a lower voltage (Figure 5b) after the rising-temperature treatment. Se−NG_{1-120} with a Dirac point at −3 V recovers n-type electron conduction because of partially restored electron delocalization at a low amount of Se−N bonds. Se−NG_{1-130} FETs nearly exhibit the same electrical properties as NG FETs with a slight decrease in carrier mobility. Reversible change in n/p-doping behavior and carrier mobility of Se−N-modified NG can be used for controlling the electrical properties of FETs.

The carrier mobility of FET devices was also studied to illustrate their controllability. We extracted the carrier mobility of NG and Se−NG_1 from the linear region of the I_{ds}−V_g curves by the following equation[47]

$$\mu = [dI_{ds}/dV_g] \times [L/W] \times [1/C_i] \times [1/V_{ds}] \quad (2)$$

where I_{ds} is the drain current; V_g is the gate voltage; dI_{ds}/dV_g is the slope of transfer characteristics (I_{ds}−V_g plot); L and W are, respectively, the channel length (2 mm) and width (0.2 mm) of the device; and C_i is the gate capacitance per unit area (~10 nF/cm^2).

The calculation result (Figure 5d) shows that n-type NG_1 exhibits a higher room-temperature hole mobility of 229.4 cm^2 V^{-1} s^{-1} than electron mobility (97.6 cm^2 V^{-1} s^{-1}). This asymmetric feature is usually caused by the scattering of ionized nitrogen impurities.[12,46] This performance is also observed for Se−NG_1. Despite that, the modification of Se−NG results in an obvious decrease in carrier mobility because the formation of Se−N bonds may introduce defects into the carbon-based conjugation structure. We evaluated the change of carrier mobility based on the following equation

$$R = [\mu_e'/\mu_e] \times 100\% \text{ or } [\mu_h'/\mu_h] \times 100\% \quad (3)$$

where μ_e' and μ_e are the electron mobility of Se−NG_1 and NG_1, respectively, and μ_h' and μ_h are the hole mobility of Se−NG_1 and NG_1, respectively. Compared to hole mobility (R = 65.56%), electron mobility decreases severely (R = 3.20%). Moreover, Se−NG_1 transformed from n-type to p-type conduction. Specifically, the p-type Se−NG_{1-30} maintains a hole mobility of 150.4 cm^2 V^{-1} s^{-1} in comparison to the extremely low electron mobility (3.1 cm^2 V^{-1} s^{-1}). Both electron and hole mobilities increased continuously owing to the cleavage of Se−N bonds (Figure 5c) through the rising-temperature treatment. Finally, Se−NG_{1-130} recover the original carrier mobility of NG_1. Our results indicate that Se−NG not only enables reversible transformation between n-type and p-type conduction but also is suitable for tuning electron or hole mobility by controlling the treated temperature. The modification via dynamic covalent bonds is a versatile method of reversibly tailoring electronic properties of 2D nanomaterials.

3. CONCLUSIONS

We synthesized a large-area (~5.0 cm), single-layer uniform NG film, which was modified by PhSeBr. XPS and Raman spectroscopy were performed to investigate the selectivity and reversibility of Se−N dynamic covalent bonds. Among all bonding characters for embedded N atoms of NG, protonated N increased whereas pyridinic N and pyrrolic N decreased. The increase in I_D/I_G from 0.69 to 0.83 and the shifts of 2D bands from 2677.6 cm^{-1} (NG) to 2679.5 cm^{-1} (Se−NG) observed by Raman spectroscopy also reveal the change in electronic interaction. Se−N dynamic covalent bonds cleave at 60−130 °C and exhibit excellent cycling performance with a slight change in the area percentage of the three different N types for no more than 7.9% after 10 cycles. Furthermore, FETs based on Se−NG show a change from n-type to p-type conduction and tunable carrier mobilities with electron and hole mobilities of 97.6 and 229.4 cm^2 V^{-1} s^{-1}, respectively, for NG and 3.1 and 150.4 cm^2 V^{-1} s^{-1}, respectively, for Se−NG. Se−NG can be used to reversibly control the electrical properties of FETs by optimizing dynamic covalent bonds on the surface.

4. EXPERIMENTAL SECTION

4.1. Materials Synthesis. The monolayer NG film was synthesized on a copper foil (25 μm) in a tube furnace using a CVD system (Anhui BEQ Equipment Technology Co., Ltd.). The copper foil (~5 × 5 cm^2) was cleaned in a volume fraction of 50% acetic acid solution and dried in Ar atmosphere. Melamine powder [100 mg (NG_1) or 150 mg (NG_2)](>99%, J&K) was placed in the first furnace of sublimation at 350 °C, whereas the copper foil (>99.99%, Alfa Aesar) was loaded into the second furnace heated at 1010 °C. Then, the quartz tube was flushed with Ar (1000 sccm, >99.999%) for 30 min to remove oxygen. Then, the second furnace was ramped up to 1030 °C at 20 °C/min with 300 sccm Ar and 100 sccm H_2 for 30 min to anneal the copper. After that, the copper foil was cooled to 1010 °C. At the same time, the first furnace was ramped up to 350 °C and held there for 20 min with 1 sccm CH_4 under atmospheric pressure. After growth, the furnace was cooled to 30 °C at 65 °C/min.

GH was prepared in the same furnace with NG. The copper foil was cleaned under the above conditions and loaded into the second furnace. Before heating, the system was flushed. Then, the second furnace was ramped up to 1030 °C at 20 °C/min with Ar (300 sccm) and H_2 (100 sccm) for 30 min to anneal the copper. After that, the copper foil was cooled to 1010 °C and held there with 1 sccm CH_4 for 20 min. After growth, the furnace was cooled to 30 °C at 65 °C/min.

DOI: 10.1021/acsami.9b02989
ACS Appl. Mater. Interfaces 2019, 11, 24360−24366

The films were transferred onto an SiO_2/Si base and TEM grids by bubbling using an aqueous solution containing NaOH. The sample was spin-coated with poly(methyl methacrylate) (PMMA, 8 wt % in anisole, 950 K molecular weight) at a rotation rate of 3000 rpm for 50 s. The PMMA-supported NG film was baked at 100 °C for 15 min and then peeled off from the copper foil through a bubbling method at room temperature. The above film was washed with deionized water to remove impurities and then extracted by the SiO_2/Si substrate or the TEM grid. To promote the adhesion between NG and PMMA, the sample was baked at 110 °C for 15 min. An acetone solution bath (30 °C for 0.5 h) was eventually used to clean the sample to remove PMMA.

4.2. Modification of NG Films. The NG_1 and NG_2 on the SiO_2/Si/SiO_2 substrates were modified with dichloromethane containing phenylselenyl bromine (PhSeBr, >98%, Alfa). After ultrasound irradiation of the NG films in the solution (0.1 mg/mL) above for no more than 1 min, they were rinsed with dichloromethane and allowed to air-dry.

After modification, the above NG films were heated at 30, 60, 90, 120, and 130 °C (termed Se−NG_{1-30}, Se−NG_{1-60}, Se−NG_{1-90}, Se−NG_{1-120}, and Se−NG_{1-130}) in a vacuum and inert atmosphere for 15 min, respectively.

4.3. Characterization. Optical microscopy (Olympus BX51M) was performed to examine the surface morphology of the NG films. Raman spectroscopy (DXR Microscope, λ = 532 nm) was used to record the structure of NG. The thickness of the NG film was acquired with AFM (Bruker, Dimension Icon). XPS characterization was recorded with a PerkinElmer PHI 3056 spectrometer. TEM (JEOL JEM-2100F operated at 80 kV) and high-resolution TEM were used to obtain information of the crystal structure of NG.

4.4. Device Fabrication and Transport Measurements. The NG films were transferred onto the SiO_2/Si substrate (with 1 μm SiO_2) for the FET mobility measurement. The contacts were annealed at 200 °C for 1 h after depositing by a thermal evaporator (Ti/Au-5 nm/50 nm). A physical property measurement system (Quantum Design DynaCool) with two Keithley 2400 source meters was used for electrical transport measurements.

■ ASSOCIATED CONTENT

Supporting Information

The Supporting Information is available free of charge on the ACS Publications website at DOI: 10.1021/acsami.9b02989.

Schematic and temperature profiles for the preparation of NG films; photos and optical micrograph of as-synthesized NG films; XPS spectra of as-synthesized NG films; TEM images and elements distribution of an as-synthesized Se−NG film; the content of bonding characters for embedded N atoms in NG and Se−NG after treatment at different temperatures; XPS spectrum of Se 3d, Br 3d, and N 1s for Se−NG; corresponding ratio of 2D-band frequency; maps of the D peak intensity for Se−NG; optical micrograph of the device; and electrical properties of Se−NG (PDF)

■ AUTHOR INFORMATION

Corresponding Authors

*E-mail: weifeng@tju.edu.cn (W.F.).
*E-mail: fengyiyu@tju.edu.cn (Y.F.).

ORCID

Yiyu Feng: 0000-0002-1071-1995
Lihong Bao: 0000-0002-2942-892X
Shixuan Du: 0000-0001-9323-1307
Huanli Dong: 0000-0002-5698-5369
Yongtao Shen: 0000-0002-4463-6436
Wei Feng: 0000-0002-5816-7343

Notes

The authors declare no competing financial interest.

■ ACKNOWLEDGMENTS

This work was financially supported by the National Key R&D Program of China (no. 2016YFA0202302), the National Natural Science Funds for Distinguished Young Scholars (no. 51425306), the State Key Program of National Natural Science Foundation of China (no. 51633007), and the National Natural Science Foundation of China (nos. 51573125, 51573147 and 51803151).

■ REFERENCES

(1) Liu, H.; Liu, Y.; Zhu, D. Chemical Doping of Graphene. *J. Mater. Chem.* **2011**, *21*, 3335−3345.

(2) Gao, L.; Ren, W.; Xu, H.; Jin, L.; Wang, Z.; Ma, T.; Ma, L. P.; Zhang, Z.; Fu, Q.; Peng, L. M.; Bao, X. H.; Cheng, H. M. Repeated Growth and Bubbling Transfer of Graphene with Millimetre-Size Single-Crystal Grains Using Platinum. *Nat. Commun.* **2012**, *3*, 699.

(3) Ambrosi, A.; Pumera, M. The CVD Graphene Transfer Procedure Introduces Metallic Impurities which Alter the Graphene Electrochemical Properties. *Nanoscale* **2014**, *6*, 472−476.

(4) Rojas, W. Y.; Winter, A. D.; Grote, J.; Kim, S. S.; Naik, R. R.; Williams, A. D.; Weiland, C.; Principe, E.; Fischer, D. A.; Banerjee, S.; Prendergast, D.; Campo, E. M. Strain and Bond Length Dynamics upon Growth and Transfer of Graphene by NEXAFS Spectroscopy From First Principles and Experiment. *Langmuir* **2018**, *34*, 1783−1794.

(5) Qin, M.; Xu, Y.; Cao, R.; Feng, W.; Chen, L. Effiiently Controlling the 3D Thermal Conductivity of a Polymer Nanocomposite via a Hyperelastic Double Continuous Network of Graphene and Sponge. *Adv. Funct. Mater.* **2018**, *28*, 1805053.

(6) Yang, Y.; Zhang, L.; Ji, X.; Zhang, L.; Wang, H.; Zhao, H. Preparation of Janus Graphene Oxide (GO) Nanosheets Based on Electrostatic Assembly of GO Nanosheets and Polystyrene Microspheres. *Macromol. Rapid Commun.* **2016**, *37*, 1520−1526.

(7) Sarkar, S.; Zhang, H.; Huang, J.-W.; Wang, F.; Bekyarova, E.; Lau, C. N.; Haddon, R. C. Organometallic Hexahapto Functionalization of Single Layer Graphene as a Route to High Mobility Graphene Devices. *Adv. Mater.* **2013**, *25*, 1131−1136.

(8) Sun, J.; Deng, Y.; Li, J.; Wang, G.; He, P.; Tian, S.; Bu, X.; Di, Z.; Yang, S.; Ding, G.; Xie, X. A New Graphene Derivative: Hydroxylated Graphene with Excellent Biocompatibility. *ACS Appl. Mater. Interfaces* **2016**, *8*, 10226−10233.

(9) Park, S.; Yun, J. M.; Maiti, U. N.; Moon, H.-S.; Jin, H. M.; Kim, S. O. Device-Oriented Graphene Nanopatterning by Mussel-Inspired Directed Block Copolymer Self-Assembly. *Nanotechnology* **2014**, *25*, 014008.

(10) Wu, H.; Yi, W.; Chen, Z.; Wang, H.; Du, Q. Janus Graphene Oxide Nanosheets Prepared via Pickering Emulsion Template. *Carbon* **2015**, *93*, 473−483.

(11) Hess, L. H.; Lyuleeva, A.; Blaschke, B. M.; Sachsenhauser, M.; Seifert, M.; Garrido, J. A.; Deubel, F. Graphene Transistors with Multifunctional Polymer Brushes for Biosensing Applications. *ACS Appl. Mater. Interfaces* **2014**, *6*, 9705−9710.

(12) Wang, Z.; Li, P.; Chen, Y.; Liu, J.; Tian, H.; Zhou, J.; Zhang, W.; Li, Y. Synthesis of Nitrogen-Doped Graphene by Chemical Vapour Deposition Using Melamine as the Sole Solid Source of Carbon and Nitrogen. *J. Mater. Chem. C* **2014**, *2*, 7396−7401.

(13) Jin, Z.; Yao, J.; Kittrell, C.; Tour, J. M. Large-Scale Growth and Characterizations of Nitrogen-Doped Monolayer Graphene Sheets. *ACS Nano* **2011**, *5*, 4112−4117.

(14) Xue, Y.; Wu, B.; Jiang, L.; Guo, Y.; Huang, L.; Chen, J.; Tan, J.; Geng, D.; Luo, B.; Hu, W.; Yu, G.; Liu, Y. Low Temperature Growth of Highly Nitrogen-Doped Single Crystal Graphene Arrays by Chemical Vapor Deposition. *J. Am. Chem. Soc.* **2012**, *134*, 11060−11063.

DOI: 10.1021/acsami.9b02989
ACS Appl. Mater. Interfaces 2019, 11, 24360−24366

(15) Li, J.; Lin, L.; Rui, D.; Li, Q.; Zhang, J.; Kang, N.; Zhang, Y.; Peng, H.; Liu, Z.; Xu, H. Q. Electron-Hole Symmetry Breaking in Charge Transport in Nitrogen-Doped Graphene. *ACS Nano* **2017**, *11*, 4641−4650.
(16) Guo, B.; Liu, Q.; Chen, E.; Zhu, H.; Fang, L.; Gong, J. R. Controllable N-Doping of Graphene. *Nano Lett.* **2010**, *10*, 4975−4980.
(17) Panchakarla, L. S.; Subrahmanyam, K. S.; Saha, S. K.; Govindaraj, A.; Krishnamurthy, H. R.; Waghmare, U. V.; Rao, C. N. R. Synthesis, Structure, and Properties of Boron- and Nitrogen-Doped Graphene. *Adv. Mater.* **2009**, *21*, 4726−4730.
(18) Kong, X.-K.; Chen, C.-L.; Chen, Q.-W. Doped Graphene for Metal-Free Catalysis. *Chem. Soc. Rev.* **2014**, *43*, 2841−2857.
(19) Wu, J.; Ma, L.; Yadav, R. M.; Yang, Y.; Zhang, X.; Vajtai, R.; Lou, J.; Ajayan, P. M. Nitrogen-Doped Graphene with Pyridinic Dominance as a Highly Active and Stable Electrocatalyst for Oxygen Reduction. *ACS Appl. Mater. Interfaces* **2015**, *7*, 14763−14769.
(20) Wang, H.; Zhou, Y.; Wu, D.; Liao, L.; Zhao, S.; Peng, H.; Liu, Z. Synthesis of Boron-Doped Graphene Monolayers Using the Sole Solid Feedstock by Chemical Vapor Deposition. *Small* **2013**, *9*, 1316−1320.
(21) Crowther, A. C.; Ghassaei, A.; Jung, N.; Brus, L. E. Strong Charge-Transfer Doping of 1 to 10 Layer Graphene by NO_2. *ACS Nano* **2012**, *6*, 1865−1875.
(22) Srivastava, P. K.; Yadav, P.; Rani, V.; Ghosh, S. Controlled Doping in Graphene Monolayers by Trapping Organic Molecules at the Graphene-Substrate Interface. *ACS Appl. Mater. Interfaces* **2017**, *9*, 5375−5381.
(23) Shin, H.-J.; Choi, W. M.; Choi, D.; Han, G. H.; Yoon, S.-M.; Park, H.-K.; Kim, S.-W.; Jin, Y. W.; Lee, S. Y.; Kim, J. M.; Choi, J.-Y.; Lee, Y. H. Control of Electronic Structure of Graphene by Various Dopants and Their Effects on a Nanogenerator. *J. Am. Chem. Soc.* **2010**, *132*, 15603−15609.
(24) Lu, M.; Nicolai, H. T.; Wetzelaer, G.-J. A. H.; Blom, P. W. M. N-Type Doping of Poly(P- phenylene vinylene) with Air-Stable Dopants. *Appl. Phys. Lett.* **2011**, *99*, 173302.
(25) Dong, X.; Fu, D.; Fang, W.; Shi, Y.; Chen, P.; Li, L.-J. Doping Single-Layer Graphene with Aromatic Molecules. *Small* **2009**, *5*, 1422−1426.
(26) Gao, Z. Q.; Mi, B. X.; Xu, G. Z.; Wan, Y. Q.; Gong, M. L.; Cheah, K. W.; Chen, C. H. An Organic p-Type Dopant with High Thermal Stability for an Organic Semiconductor. *Chem. Commun.* **2008**, 117−119.
(27) Schedin, F.; Geim, A. K.; Morozov, S. V.; Hill, E. W.; Blake, P.; Katsnelson, M. I.; Novoselov, K. S. Detection of Individual Gas Molecules Adsorbed on Graphene. *Nat. Mater.* **2007**, *6*, 652−655.
(28) Wei, P.; Liu, N.; Lee, H. R.; Adijanto, E.; Ci, L.; Naab, B. D.; Zhong, J. Q.; Park, J.; Chen, W.; Cui, Y.; Bao, Z. Tuning the Dirac Point in CVD-Grown Graphene through Solution Processed n-Type Doping with 2-(2-methoxyphenyl)-1,3-dimethyl-2,3-dihydro-1 *H*-benzoimidazole. *Nano Lett.* **2013**, *13*, 1890−1897.
(29) Rowan, S. J.; Cantrill, S. J.; Cousins, G. R. L.; Sanders, J. K. M.; Stoddart, J. F. Dynamic Covalent Chemistry. *Angew. Chem., Int. Ed.* **2002**, *41*, 898−952.
(30) Zhou, W.; Wang, L.; Li, F.; Zhang, W.; Huang, W.; Huo, F.; Xu, H. Selenium-Containing Polymer@Metal-Organic Frameworks Nanocomposites as an Efficient Multiresponsive Drug Delivery System. *Adv. Funct. Mater.* **2017**, *27*, 1605465.
(31) Yi, Y.; Xu, H.; Wang, L.; Cao, W.; Zhang, X. A new Dynamic Covalent Bond of Se-N: Towards Controlled Self-Assembly and Disassembly. *Chem.—Eur. J.* **2013**, *19*, 9506−9510.
(32) Jang, S. K.; Jang, J.-r.; Choe, W.-S.; Lee, S. Harnessing Denatured Protein for Controllable Bipolar Doping of a Monolayer Graphene. *ACS Appl. Mater. Interfaces* **2015**, *7*, 1250−1256.
(33) Ryu, S.; Liu, L.; Berciaud, S.; Yu, Y.-J.; Liu, H.; Kim, P.; Flynn, G. W.; Brus, L. E. Atmospheric Oxygen Binding and Hole Doping in Deformed Graphene on a SiO_2 Substrate. *Nano Lett.* **2010**, *10*, 4944−4951.
(34) Iqbal, M. Z.; Khan, M. F.; Iqbal, M. W.; Eom, J. Tuning the Electrical Properties of Exfoliated Graphene Layers Using Deep Ultraviolet Irradiation. *J. Mater. Chem. C* **2014**, *2*, 5404−5410.
(35) Iqbal, M. Z.; Iqbal, M. W.; Khan, M. F.; Eom, J. Ultraviolet-Light-Driven Doping Modulation in Chemical Vapor Deposition Grown Graphene. *Phys. Chem. Chem. Phys.* **2015**, *17*, 20551−20556.
(36) Velez-Fort, E.; Mathieu, C.; Pallecchi, E.; Pigneur, M.; Silly, M. G.; Belkhou, R.; Marangolo, M.; Shukla, A.; Sirotti, F.; Ouerghi, A. Epitaxial Graphene on 4H-SiC(0001) Grown under Nitrogen Flux: Evidence of Low Nitrogen Doping and High Charge Transfer. *ACS Nano* **2012**, *6*, 10893−10900.
(37) Sun, Z.; Yan, Z.; Yao, J.; Beitler, E.; Zhu, Y.; Tour, J. M. Growth of Graphene from Solid Carbon Sources. *Nature* **2010**, *468*, 549−552.
(38) Babichev, A. V.; Rykov, S. A.; Tchernycheva, M.; Smirnov, A. N.; Davydov, V. Y.; Kumzerov, Y. A.; Butko, V. Y. Influence of Substrate Microstructure on the Transport Properties of CVD-Graphene. *ACS Appl. Mater. Interfaces* **2016**, *8*, 240−246.
(39) Ferrari, A. C.; Meyer, J. C.; Scardaci, V.; Casiraghi, C.; Lazzeri, M.; Mauri, F.; Piscanec, S.; Jiang, D.; Novoselov, K. S.; Roth, S.; Geim, A. K. Raman Spectrum of Graphene and Graphene Layers. *Phys. Rev. Lett.* **2006**, *97*, 187401.
(40) Matanovic, I.; Artyushkova, K.; Strand, M. B.; Dzara, M. J.; Pylypenko, S.; Atanassov, P. Core Level Shifts of Hydrogenated Pyridinic and Pyrrolic Nitrogen in the Nitrogen-Containing Graphene-Based Electrocatalysts: In-Plane vs Edge Defects. *J. Phys. Chem. C* **2016**, *120*, 29225−29232.
(41) Mugesh, G.; Panda, A.; Singh, H. B.; Butcher, R. J. Intramolecular Se...N Nonbonding Interactions in Low-Valent Organoselenium Derivatives: A Detailed Study by 1H and 77Se NMR Spectroscopy and X-ray Crystallography. *Chem.—Eur. J.* **1999**, *5*, 1411−1421.
(42) Xie, M.; Wang, L.; Liu, F.; Zhang, D.; Gao, J. Dynamic Conversion Between Se-N Covalent and Noncovalent Interactions. *J. Phys. Chem. A* **2016**, *120*, 9081−9088.
(43) Wang, H.; Maiyalagan, T.; Wang, X. Review on Recent Progress in Nitrogen-Doped Graphene: Synthesis, Characterization, and Its Potential Applications. *ACS Catal.* **2012**, *2*, 781−794.
(44) Lim, H.; Lee, J. S.; Shin, H.-J.; Shin, H. S.; Choi, H. C. Spatially Resolved Spontaneous Reactivity of Diazonium Salt on Edge and Basal Plane of Graphene without Surfactant and Its Doping Effect. *Langmuir* **2010**, *26*, 12278−12284.
(45) Georgakilas, V.; Otyepka, M.; Bourlinos, A. B.; Chandra, V.; Kim, N.; Kemp, K. C.; Hobza, P.; Zboril, R.; Kim, K. S. Functionalization of Graphene: Covalent and Non-Covalent Approaches, Derivatives and Applications. *Chem. Rev.* **2012**, *112*, 6156−6214.
(46) Lu, Y.-F.; Lo, S.-T.; Lin, J.-C.; Zhang, W.; Lu, J.-Y.; Liu, F.-H.; Tseng, C.-M.; Lee, Y.-H.; Liang, C.-T.; Li, L.-J. Nitrogen-Doped Graphene Sheets Grown by Chemical Vapor Deposition: Synthesis and Influence of Nitrogen Impurities on Carrier Transport. *ACS Nano* **2013**, *7*, 6522−6532.
(47) Wei, D.; Liu, Y.; Wang, Y.; Zhang, H.; Huang, L.; Yu, G. Synthesis of N-Doped Graphene by Chemical Vapor Deposition and Its Electrical Properties. *Nano Lett.* **2009**, *9*, 1752−1758.

DOI: 10.1021/acsami.9b02989
ACS Appl. Mater. Interfaces 2019, 11, 24360−24366